Observed and CAM3 GCM Sea Surface Wind Speed Distributions: Characterization, Comparison, and Bias Reduction

SCOTT B. CAPPS AND CHARLES S. ZENDER

University of California, Irvine, Irvine, California

(Manuscript received 10 December 2007, in final form 8 April 2008)

ABSTRACT

Climatological surface wind speed probability density functions (PDFs) estimated from observations are characterized and used to evaluate, for the first time, contemporaneous wind PDFs predicted by a GCM. The observations include NASA's global Quick Scatterometer (QuikSCAT) dataset, the NCEP/Department of Energy Global Reanalysis 2 (NCEP-2) 6-hourly reanalysis, and the Tropical Atmosphere Ocean (TAO)/Triangle Trans-Ocean Buoy Network (TRITON) moored buoy data, all from 2000 to 2005. Wind speed mean, 90th percentile, standard deviation, and Weibull shape parameter climatologies are constructed from these data. New features that emerge from the analysis include the identification of a stationary pattern to the wind speed variance in the equatorial Pacific. Interestingly, a distinct wind speed shape anomaly migrates with the ITCZ across this stationary background.

The GCM despite its coarser spatial and temporal resolution predicts wind speed PDFs in general agreement with observations. Relative to QuikSCAT, the NCAR Community Atmosphere Model, version 3 (CAM3) GCM has a globally averaged positive mean wind speed bias of about 0.2 $m\,s^{-1}$ originating primarily within the trades and Southern Hemisphere storm track. Global standard deviation biases are largest in the winter hemisphere storm tracks. The largest shape biases occur along the equatorial peripheries of the Northern Hemisphere and southern Indian Ocean anticyclones. Year-round negative shape and mean wind speed biases persist along the ITCZ. The GCM's overactive tropical convection and slight subtropical anticyclone displacement contribute to positive mean speed, standard deviation, and shape trade biases.

Surface heat and energy fluxes depend nonlinearly on wind speed magnitude, are sensitive to the tails of the wind distribution, and hence vary significantly on spatiotemporal scales not resolved by GCMs. Limited computing resources force the use of coarse-resolution GCMs, which do not resolve finer-scale wind speed fluctuations. Rather, surface fluxes are determined from the mean wind speed computed by averaging spatially and temporally over subgrid-scale features. Some surface flux routines account for gustiness during low mean winds resulting from thermally driven convection. The authors hypothesize that GCMs systematically underestimate surface momentum flux nonlinearities and that this biases surface wind predictions most in regions of strong winds with high variability. To test this, climate simulations that account for surface fluxes due to subgrid-scale GCM winds are performed. This significantly improves climatological surface wind speed statistics, particularly in the Southern Hemisphere storm track, consistent with the hypothesis. These wind speed improvements can be attributed to a reduction in GCM sea level pressure biases throughout the globe.

1. Introduction

Surface winds are vital to global climate, driving ocean currents and initiating convection through surface convergence, divergence, and heat and moisture transfer. Winds impart stress onto the underlying surface, influence air–sea energy and gas fluxes, and advect chemical species (Wanninkhof et al. 2002; Donelan et al. 2002). It is important for models to predict the wind probability density function (PDF) in regimes where surface momentum, energy, and gas fluxes depend nonlinearly on wind speed (Wang et al. 1998; Feely et al. 2004).

Scatterometer measurements offer the opportunity to characterize wind speed PDFs across climatically significant spatial and temporal scales. Monahan (2006a) first examined global sea surface wind speed PDFs

Corresponding author address: Scott B. Capps, Department of Earth System Science, University of California, Irvine, Irvine, CA 92697–3100.
E-mail: scapps@uci.edu

DOI: 10.1175/2008JCLI2374.1

from satellite measurements on climatological time scales. He intercompared global ocean wind PDFs estimated from the Quick Scatterometer (QuikSCAT) with PDFs constructed from blended Special Sensor Microwave Imager (SSM/I) measurements and European Centre for Medium-Range Weather Forecasts (ECMWF) analysis, National Centers for Environmental Prediction (NCEP) reanalysis, and in situ National Data Buoy Center (NDBC) observations. Two-parameter PDFs, such as Weibull distributions, accurately represent these wind speed data (Monahan 2006a,b). Our study extends Monahan (2006a) by utilizing recently reprocessed QuikSCAT measurements, consid ering more regional [Tropical Atmosphere Ocean (TAO)/Triangle Trans-Ocean Buoy Network (TRITON) measurements] and seasonal aspects of wind variability, and using these results to evaluate and interpret GCM wind biases. Further, we demonstrate that resolving surface wind speed PDFs improves GCM surface wind predictions. In addition to thermodynamic scalar gradients, atmospheric surface layer flux bulk formulas are dependent upon surface wind speed magnitude. Because ultimately we are interested in surface fluxes, this study characterizes wind speed magnitude PDFs. Other studies have characterized observed PDFs of wind vector zonal and meridional components (Monahan 2006a).

Although wind gusts in excess of 15 m s^{-1} are observed only 5% of the time, they have a large impact on cyclogenesis within the storm track regions. Yuan (2004) intercompared QuikSCAT, NCEP–National Center for Atmospheric Research (NCAR) reanalysis, and ECMWF operational archive surface analysis data wind statistics and found climatalogically significant slower NCEP–NCAR and ECMWF maximum wind speeds within the Southern Hemisphere storm track. Storm track intensity and surface kinetic energy fluxes within NCEP–NCAR and ECMWF are greatly underestimated as a result. Our study characterizes the 2000–05 global distribution of the wind speed mean, 90th percentile, standard deviation, and shape parameter.

This study has three goals. First, we seek to characterize agreement among three recent datasets [QuikSCAT, NCEP/Department of Energy Global Reanalysis 2 (NCEP-2), and TAO/TRITON] that provide independent estimates of surface wind PDFs. As an in situ measurement network, TAO/TRITON also provides the additional information necessary to estimate surface flux PDFs, which we will assess in a future study. Second, we wish to characterize GCM predictions against these observations to identify regions and seasons where fast time-scale and/or fine spatial scale wind variability may contribute significantly to surface fluxes, and thus the local climate state. This will help us quantify the importance of representing subgrid-scale wind variability in models, that is, in predicting the wind PDF in addition to the mean wind. Third, we show that prescribing (with the goal of eventually predicting) the wind speed PDF improves GCM surface wind predictions. This is attributed to the nonlinear momentum flux response to subgrid-scale wind speed variability.

The paper proceeds as follows: Section 2 describes the datasets, GCM, and analysis techniques. Model biases will be quantified through a surface wind speed PDF comparison globally (section 3) and regionally in the storm track (section 3a), trade winds (section 3b), South Asian monsoon (section 3c), and TAO/TRITON (section 3d) regions. Improved predictions in these regions will be shown to result from the representation of subgrid-scale wind speed PDFs within the model (section 4). The implications of this study for future research and our conclusions are summarized in sections 5 and 6.

2. Methods

a. SeaWinds on QuikSCAT

The two operational satellite-borne scatterometers are the European Space Agency's Remote Sensing Satellite (ERS, launched 1993) and NASA's SeaWinds on board QuikSCAT (launched mid-1999). Here we analyze QuikSCAT data, which has comparable accuracy (Bentamy et al. 2000) but higher spatial resolution (0.25° × 0.25° versus 0.5° × 0.5°) and a wider swath (1800 km versus 500 km), allowing for 93% daily coverage. QuikSCAT measures surface stress twice daily (approximately 0600 and 1800 LST), with the primary goal of estimating global ocean surface winds (Hoffman and Leidner 2005). Comparisons of QuikSCAT with in situ buoy and ship-based measurements place QuikSCAT accuracy at approximately 1 m s^{-1} with a slight overestimation at high wind speeds (Ebuchi et al. 2002; Bourassa et al. 2003; Chelton and Freilich 2005). Level 3 QuikSCAT data, available since 19 July 1999, were reprocessed in 2006 to improve flagging of rain contamination and performance at high speeds. We use the 6-yr (January 2000–December 2005) level 3 reprocessed QuikSCAT 10-m surface wind speed climatology. Temporal wind speed PDFs are calculated at each of the wind vector cells across the entire time period. To intercompare with the GCM, these temporal statistics are regridded to the horizontal resolution (T85) of the GCM (described below). Wind vector cells containing the possibility of rain were not included in this study.

There are intrinsic differences between scatterometer-derived winds and GCM-predicted surfaces winds.

QuikSCAT detects surface wind stress from ocean roughness. The 10-m wind velocity is then estimated using a retrieval algorithm that assumes a neutrally stable atmosphere. This assumption (Hoffman and Leidner 2005) introduces a bias during nonneutral conditions and is not remedied in this study. Mears et al. (2001) and Chelton and Freilich (2005) found that 10-m anemometer winds are typically 0.2 m s^{-1} slower than in situ 10-m neutral-stability winds. Moreover, the retrieved 10-m wind is relative to the underlying ocean current and is the correct wind velocity to employ when calculating air–sea exchange. However, most GCMs predict winds relative to a fixed location. Thus, fast surface ocean currents can cause differences up to 1 m s^{-1} between modeled and QuikSCAT wind speeds (Kelly et al. 2001; Chelton and Freilich 2005). Kelly et al. (2001) found differences between QuikSCAT and buoys of 0.5 m s^{-1} over the slower tropical Pacific equatorial currents. TAO/TRITON buoy winds used in this study (section 2c) are relative to climatological zonal ocean surface currents (Kelly et al. 2005).

b. The Community Atmosphere Model

The GCM we employ is the Community Atmosphere Model, version 3 (CAM3) (Collins et al. 2006a), the atmospheric component of the NCAR Community Climate System Model (CCSM). Simulations are performed at the standard T85 resolution (approximately 1.4° × 1.4° equatorial with 26 levels) and the Eulerian spectral dynamical core. Observed annually varying monthly mean sea surface temperatures (SSTs) and ice concentrations from 2000 to 2005 (Reynolds et al. 2002) bound the atmospheric model over the oceans. The GCM linearly interpolates the midmonth values provided by the SST dataset to obtain instantaneous SSTs. For each time step (10 min) the GCM predicts surface layer winds and interpolates them to 10 m with an iterative approach (Collins et al. 2004) that accounts for atmospheric stability and ocean roughness. We subsample the instantaneous GCM predictions at QuikSCAT overflight times (approximately 0600 and 1800 LST) before intercomparing the data. Sea ice regions within the GCM (typically poleward of 60°) were removed from this study to prevent erroneous QuikSCAT versus GCM differences owing to scatterometer retrieval problems near sea ice.

c. TAO/TRITON array

Data from the 66 Autonomous Temperature Line Acquisition System (ATLAS) and TRITON buoys were obtained from the Pacific Marine Environmental Laboratory (PMEL). The TAO buoys report 6-min- (standard ATLAS) and 10-min- (next-generation ATLAS) average winds from 2-Hz measurements. We convert TRITON and ATLAS measurements within 20-min windows of the 0600 and 1800 local time QuikSCAT overflights to 10-m wind speeds assuming neutral stability using the approach of Liu and Tang (1996). This procedure requires simultaneous measurements of air temperature, humidity, or SST. Sampling points missing any of these inputs were discarded. Missing surface pressure measurements were converted to 1010 mb, following Mears et al. (2001). Zonal wind vector components are relative to climatological zonal ocean surface currents following Kelly et al. (2005). Linear interpolation between monthly Southern Oscillation index means provide daily values for the Kelly et al. formulation. The TAO data are bilinearly interpolated to T85 horizontal resolution.

d. NCEP-2

We also examine wind PDFs built from the four times daily 6-h forecast 10 m surface wind data from the NCEP-DOE AMIP-II reanalysis (Kanamitsu et al., 2002). Given the coarse temporal resolution we convert NCEPII measurements within 6-h windows of the 0600 and 1800 local time QuikSCAT overflights. These PDFs are then regridded from T62-horizontal resolution to T85-horizontal resolution.

e. Weibull PDF

The two-parameter Weibull probability density function can closely approximate the observed surface wind speed distribution (Justus et al. 1979; Pavia and O'Brien 1986; Monahan 2006b). Like the gamma distribution, the Weibull PDF is bounded by zero on the left and is fitted using shape and scale parameters. Both parameters modify the height and sharpness of the PDF peak and stretch or compress the PDF breadth. The shape parameter varies nearly linearly with the mean wind speed $\overline{U}$ and inversely with the standard deviation σ,

$$k \approx (\overline{U}/\sigma)^{1.086}. \quad (1)$$

The skewness (PDF asymmetry) and kurtosis (PDF peak sharpness; tail thickness) are both unique functions of shape. Skewness varies inversely with shape, becoming negative for shape values greater than 3.6 (Monahan 2006a). Kurtosis decreases sharply to 0 as shape increases to 2, staying close to zero for shape values greater than 2. Weibull PDFs fit well the QuikSCAT-estimated 2005 wind speed distribution for two climatologically distinct locations (Fig. 1). Regions with moderate and persistent winds, such as the trades,

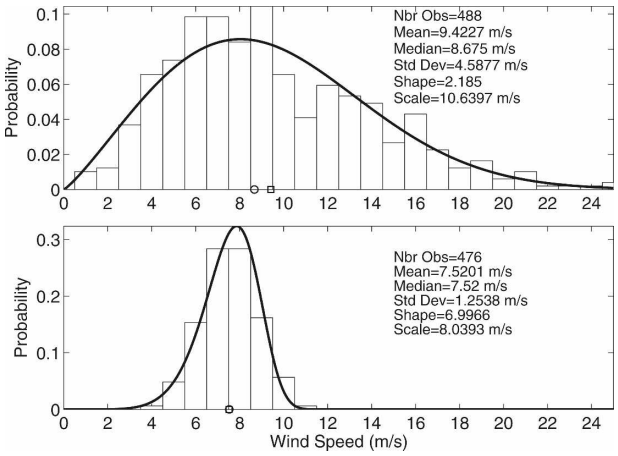

FIG. 1. 2005 QuikSCAT wind histograms and best Weibull PDF fits for a (top) storm track and (bottom) trade wind location. Squares on horizontal axis indicate mean and circles, median values.

have a relatively high shape value in comparison to gusty storm track regions. The Weibull scale parameter is similar to, and within about 10% of, the mean wind speed $\overline{U}$ (Gillette and Passi 1988) that, as a more familiar and intuitive metric, we show in our results.

3. Results

The 2000–05 climatological mean surface wind speed PDFs derived from QuikSCAT measurements demonstrate the spatial variation of the wind speed mean $\overline{U}$, its temporal variability (shown as standard deviation σ), Weibull shape parameter k [Eq. (1)], and 90th percentile wind U_{90} (Fig. 2, row 1, columns 1–4, respectively). For both NCEP-2 and CAM3, biases are determined relative to QuikSCAT. The statistical significance of CAM − QuikSCAT biases is tested applying the Student's t test to a monthly resolution time series (5% level of significance). NCEP-2 is the second observationally based estimate of global surface winds (Fig. 2, second row). NCEP-2 has faster and more variable winds in the high latitudes and matches or underestimates QuikSCAT in the tropics.

The global mean NCEP-2 wind speed is 0.4 m s^{-1} faster than QuikSCAT with the difference greatest in the storm tracks. The NCEP-2 wind speed standard deviation and 90th percentile statistics are larger in the storm tracks and trades. NCEP-2 underestimates Weibull shape values throughout the tropics and midlatitudes and matches QuikSCAT in the storm tracks.

The spatial structure of the GCM biases can, in many cases, be identified with underlying climatological wind regimes. GCM surface ocean winds are on average 0.21 m s^{-1} faster than QuikSCAT (Fig. 2). Most of these faster GCM winds are statistically significant and reside in the storm track regions of both hemispheres and in the Northern Hemisphere (NH) trade wind regions. These are consistent with surface stress biases found when comparing the GCM to ERS measurements (Collins et al. 2006b). GCM mean wind speeds within the Southern Hemisphere (SH) trade wind regions are slightly faster than for QuikSCAT [also consistent with Collins et al. (2006b)]. The GCM winds are too slow (by up to 3 m s^{-1}) in the doldrums relative to QuikSCAT and agree better with NCEP-2 winds in this region. QuikSCAT data are fewest in the doldrums where intertropical convergence zone (ITCZ) precipitation often contaminates wind retrievals (Monahan 2006a, his Fig. 4). We speculate that QuikSCAT-based wind retrievals may be too fast in the ITCZ if they sample winds outside precipitating clouds and miss the convergent winds under precipitating clouds.

Relative to QuikSCAT, the GCM winds are too variable in most regions (Fig. 2). The global mean standard deviation bias is about 0.10 m s^{-1}, with the majority of this excess variability found in the Atlantic storm track, the Pacific and Atlantic trade wind regions, and along the periphery of the Southern Ocean circumpolar region. GCM variability is underestimated near the NH western boundary currents. Within these regions, SST fronts and oceanic eddies create subgrid-scale spatial inhomogeneities in the atmospheric surface layer stability and wind variability.

The Weibull shape parameter [Eq. (1)] depends on both the mean and the standard deviation of the wind speed. The global mean GCM shape parameter bias is −0.10, with the largest discrepancies found along the ITCZ where GCM winds are too slow and too variable (Fig. 2). The GCM significantly overestimates the shape parameter just poleward of the ITCZ. The small annual mean shape parameter biases in the storm track regions are the net sums of larger seasonal oscillations (not shown) between positive and negative biases in the winter and summer storm tracks, respectively.

The zonal mean of these statistics further reveals the distinction between the mostly negative tropical model biases and the mostly small or positive extratropical biases (Fig. 4). Zonal mean shape biases are near zero or slightly positive in the subtropics and storm track regions. Negative shape biases near the equator suggest a more positively skewed GCM wind speed PDF with respect to QuikSCAT.

a. Storm-track regions

Cyclogenesis causes dramatic shifts in atmospheric stability and vertical momentum transport that lead to

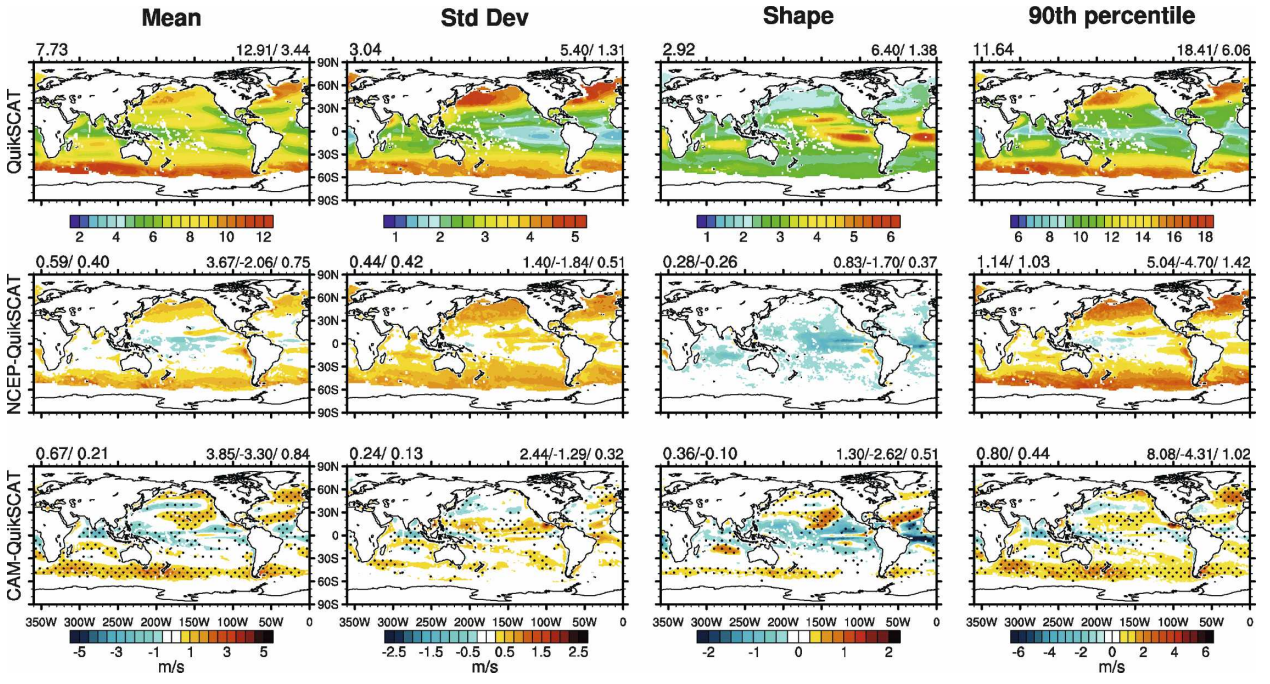

FIG. 2. (top) QuikSCAT 2000–05 mean 10-m ocean surface wind speed, standard deviation, Weibull shape, and 90th percentile. Differences (middle) NCEP-2 − QuikSCAT and (bottom) CAM3 − QuikSCAT. (top left) Mean absolute bias/mean bias and (top right) max/min/RMSE. Stippling indicates 5% level of significance.

relatively high mean wind speeds and variability. This is evident in the midlatitude storm track regions. GCM climatological surface ocean winds are between 1 and 3 m s^{-1} faster than for QuikSCAT near 50° in the Southern Ocean circumpolar region and North Pacific and Atlantic storm tracks (Fig. 2). The strong underlying ocean currents, such as the North Atlantic drift and Antarctic Circumpolar Current, may contribute a portion of these biases (section 2a).

Extreme wind speeds within the storm tracks create dynamic nonlinear responses in momentum flux. Drag imposed at the air–sea interface can act as a sink or source of atmospheric and oceanic momentum affecting wind speeds, mixed layer depths, and ocean currents. The SH storm track wind speed biases are consistent with well-documented westerly surface wind stress biases in this GCM (Hurrell et al. 2006; Collins et al. 2006b; Hack et al. 2006). These biases are linked to sea level pressure (SLP) and to surface drag. Large (<-8 hPa) SH winter SLP biases are found throughout the circumpolar region south of 50°S (e.g., Figs. 1 and 13 of Hurrell et al. 2006). The too strong meridional pressure gradient contributes to enhanced westerlies.

We believe that a second major factor that contributes to wind speed biases is the inadequate representation of wind speed variability within GCM grid cells. Air–sea momentum flux is a function of surface layer stability and ocean surface roughness. When all other properties are held constant, stronger ocean surface winds drive significantly nonlinear responses in momentum fluxes (Fig. 3). Sensible and latent heat flux increases with wind speed are much more linear than momentum flux increases. The momentum flux nonlinearity is convex, such that momentum fluxes increase more per unit wind speed as wind speed increases (Wright and Thompson 1983). The convex shape of the surface drag response to stronger winds dictates that the momentum flux computed from the full wind speed distribution is greater than that computed from the mean wind speed alone.

This suggests that representing subgrid-scale wind speed variability within a GCM would increase the global surface momentum flux. To test this, we used four equal-probability wind speed bins to better resolve the CAM3 subgrid-scale wind distribution. The experimental CAM3 is configured identical to that described above (section 2b). However, a spatial (within each T85 grid cell) and temporal (over each 10-min time step) wind speed distribution is now approximated using the Weibull PDF (section 2e). We prescribe a shape parameter proportional to the gridcell mean wind speed using the formulation by Justus et al. (1978),

$$k = C_k \sqrt{\overline{U}}, \tag{2}$$

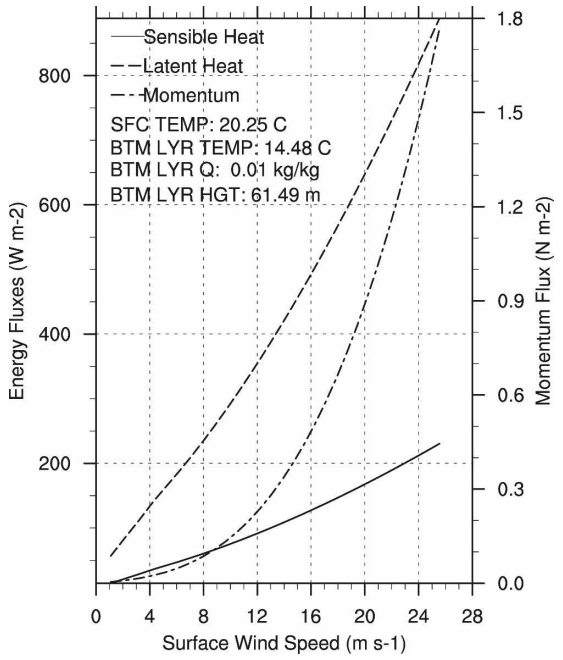

FIG. 3. Ocean surface energy and momentum flux dependence on wind speed as used in CAM3.

where C_k is 1.05, 0.94, and 0.83 for low, average, and high variability, respectively. The scale parameter is a function of k and $\overline{U}$,

$$c = \frac{\overline{U}}{\Gamma(1 + 1/K)}, \tag{3}$$

where Γ is the complete gamma function.

Our experiment divides the PDF fitted above into four equal-probability bins. For a more detailed explanation on how equal-probability wind speed bins and mean winds are calculated see the appendix [(A5)]. Each wind speed bin contains a truncated portion of the Weibull PDF. Using this truncated PDF, a mean wind speed can be calculated for each bin. The mean wind speed for each truncated PDF is equal to the first moment of the truncated PDF normalized by the wind speed interval probability [see (A5)]. Over all surfaces the experimental CAM computes the instantaneous surface momentum and energy fluxes at every time step using the mean wind speed of each of the four bins. The total flux at each grid point and time step is the average of the four bin fluxes. The experimental and control versions of CAM differ only in how the surface fluxes are computed.

Our sensitivity study shows that CAM3 momentum fluxes from the four-bin PDFs exceed the fluxes from the unresolved (i.e., one bin) PDFs (Fig. 4). Partially resolving (with four equally weighted bins) the surface wind PDF increases the climatological June 2000–05 momentum flux 13%–24% over most regions. Section 4 examines the impact these instantaneous forcings have on atmospheric circulation when allowed to feed back throughout the climate.

GCM zonal mean winds are faster by 1.4 and 1.8 m s^{-1} within the storm tracks near 50°S and 55°N, respectively (Fig. 5). These correspond to relative biases of 12% and 16%, respectively (Fig. 4). Similar differences exist between NCEP-2 and QuikSCAT within the storm track regions (Fig. 2). Larger climatological 90th percentile wind speed and standard deviation biases occur in the Atlantic storm track region than in the Pacific (Fig. 2). The underlying North Atlantic Current (section 2a) may contribute to this bias.

The largest seasonal biases in the standard deviation and 90th percentile wind speed occur in the winter storm tracks. These seasonal biases (not shown) are up to 1 and 5 m s^{-1}, respectively. The GCM overestimation of the 90th percentile winds within the seasonal storm tracks is in contrast to the ECMWF GCM, which has the opposite bias relative to QuikSCAT (Yuan 2004). These storm track wind biases may both manifest and result from biases in surface fluxes and cyclone intensity (Yuan 2004).

The overestimated winter and underestimated summer wind speed variances nearly offset each other and produce relatively small zonal mean climatological biases of 0.25 (5% departure) and 0.1 m s^{-1} (2% departure) in the NH and SH storm tracks, respectively (Fig. 5).

Vertical momentum transport within the ABL over warmer SSTs reduces vertical wind shear, resulting in faster surface winds (Chelton et al. 2004). Conversely, suppression of vertical momentum transport over cooler SSTs results in slower surface winds and faster winds aloft. The resulting finescale horizontal wind field divergence and vorticity patterns can further induce vertical mixing within the ABL. Thus, GCM wind speed biases near SST fronts are highly influenced by the temporal and spatial resolution of the SST boundary dataset. The west-to-east finger of statistically significant excessive GCM climatological wind speed mean, variability, and 90th percentile statistics near the SST front off the eastern coast of South Africa (39 °S) is of particular interest (Fig. 2). This is where the Agulhas Current meets the Circumpolar Current. The prescribed GCM SST dataset underestimates SST gradients and subgrid-scale meanders of the SST front in this region (O'Neill et al. 2005). Smaller SST gradients should result in smaller horizontal pressure gradients and surface winds, yet the GCM has too strong mean

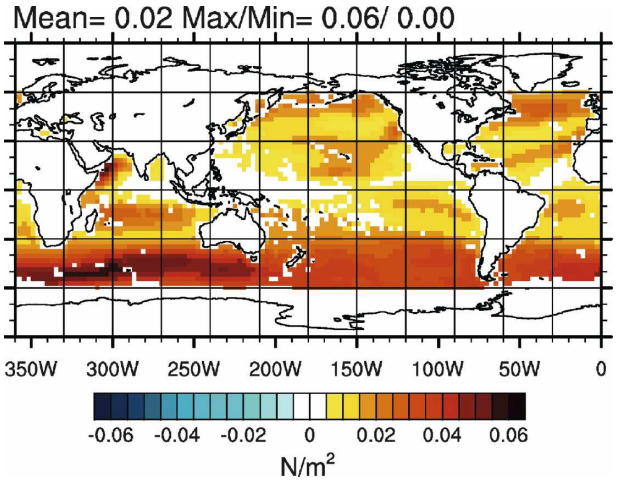

FIG. 4. Sensitivity of mean 2000–05 June momentum fluxes to representation of subgrid-scale winds. Difference shows CAM3 predictions with four wind bins per grid cell minus standard one-bin predictions.

and 90th percentile wind speeds and higher variability in this region.

The GCM and QuikSCAT shape values agree relatively well in the NH storm tracks. This is expected from (1) given the collocated positive mean and standard deviation biases (Fig. 2). A climatological mean shape parameter bias of 0.75 stretches from New Zealand south of Australia (Fig. 2), coincident with the greatest SLP gradient bias (Fig. 1 of Hurrell et al. 2006). This shape parameter bias reaches about 1 during the SH spring.

b. *Trade wind regions*

Trade wind regions appear as the elongated oval-shaped areas along the equatorial periphery of the subtropical anticyclones containing moderate mean wind speeds (7–8 m s^{-1}), low standard deviations (1 m s^{-1}), and relatively high shape values (6–7) (Fig. 2).

GCM climatological winds are predominantly faster with higher shape values in the trade wind regions, consistent with subtropical SLP biases. Differences in the strength and location of the northern Pacific and Atlantic summer subtropical anticyclones result in SLP biases as high as 8 and 3 hPa, respectively (Figs. 1 and 2 of Hurrell et al. 2006). These positive SLP biases decrease during NH winter to 5 and 1 hPa, respectively. SLP biases in the SH subtropics are smaller and less seasonal than in the NH, consistent with the smaller seasonal migration of the SH storm track and anticyclone.

Coincident with the SLP biases, NH speed and shape differences are largest during the late NH spring and summer months when the trade wind regimes reach their northernmost location (Fig. 6). The mean trade wind speed biases are smaller in the SH than the NH in most months in all three ocean basins. The largest SH trade wind shape biases (exceeding 3) occur in August–October. Two bands of large positive shape biases straddle the equatorial Pacific from June to November. Surface wind convergence studies have confirmed the existence of a double ITCZ in the eastern equatorial Pacific (Liu and Xie 2002). Surface wind convergence within the southern ITCZ is a result of wind speed deceleration while flowing from warmer to colder SSTs. Thus, strong SST gradients and differing atmospheric stability regimes associated with the subgrid-scale equatorial cold tongue could contribute to these biases.

The GCM exaggerates the persistence and mean speed of the northerly winds along the Californian

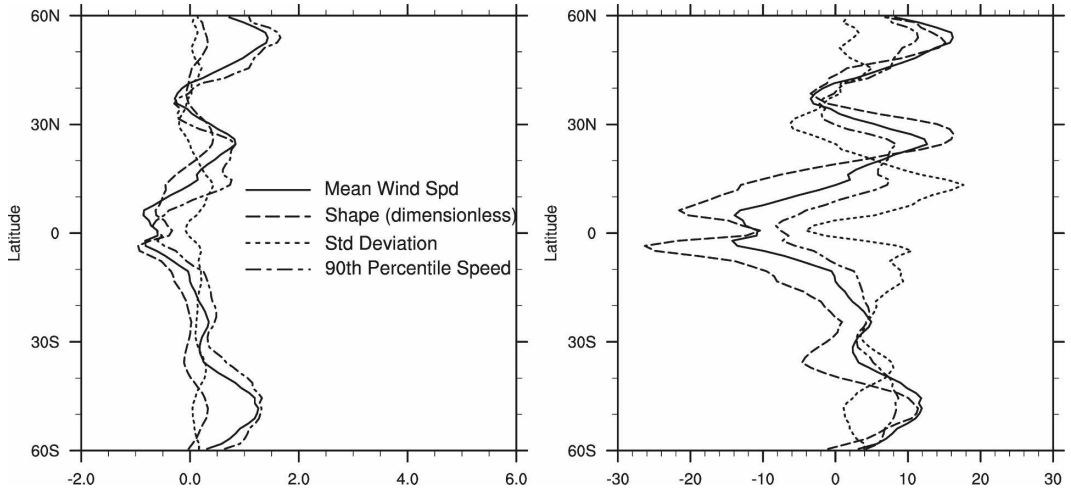

FIG. 5. Zonal profile of CAM − QuikSCAT (left) surface wind statistic biases and (right) differences as a percentage of zonal mean observed values.

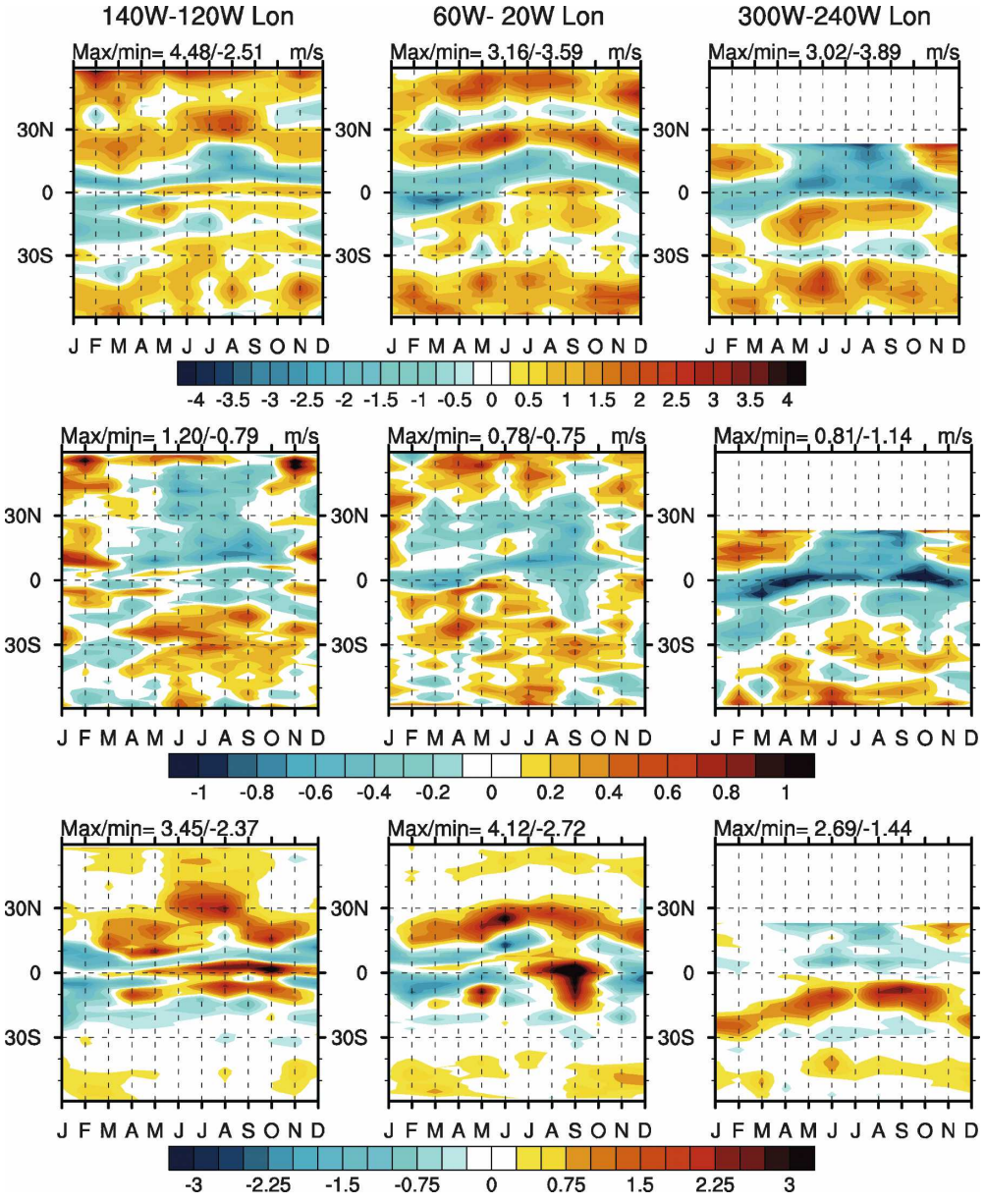

FIG. 6. Monthly zonal mean near-surface (top) mean wind speed, (middle) standard deviation, and (bottom) shape biases (CAM − QuikSCAT) for (left) Pacific, (middle) Atlantic, and (right) Indian Ocean.

coast between the NH summer Pacific high and the desert southwest heat low (Figs. 6, far left). Positive mean wind speed biases on the order of 3 m s^{-1} (not shown) exist along the equatorial flank of both NH anticyclones in NH summer. These biases along with collocated negative standard deviation biases result in significant shape biases exceeding 4 (Fig. 7). Similar biases exist in the northern Atlantic. Thus, a crescent swath of positive mean wind speed, shape, and negative standard deviation biases migrate meridionally in a seasonal rhythm along the equatorial flanks of the Pacific and Atlantic anticyclones (Figs. 6). During the NH winter months, these swaths stretch zonally across the basins, containing smaller biases of approximately 1 m s^{-1} and 1, respectively.

A swath of positive shape biases of about 2 persists through the year in the southern Indian Ocean, reaching a peak of 2.4 during SH spring (Figs. 7 and 6). This and the collocated faster mean winds (not shown) are likely related to a GCM meridional pressure gradient overestimate in the same region (Hurrell et al. 2006).

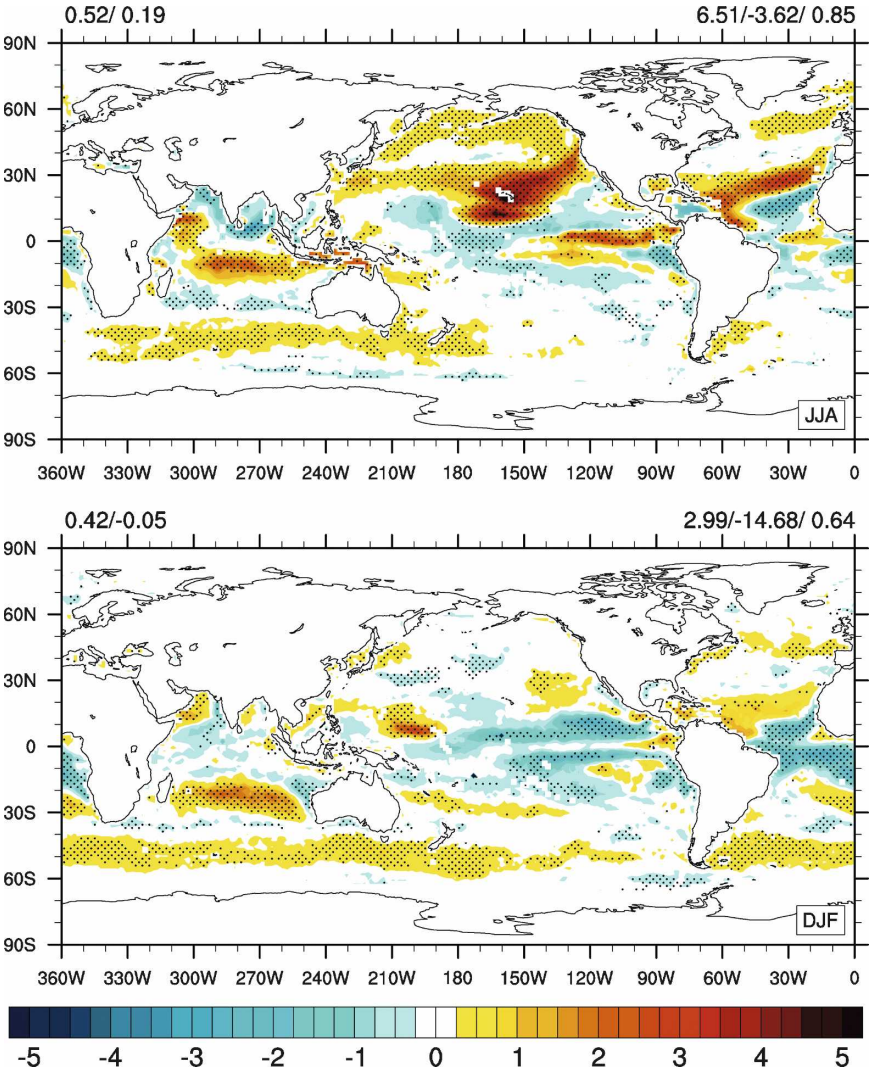

FIG. 7. Northern Hemisphere (top) summer and (bottom) winter global climatological shape biases (CAM − QuikSCAT). (top left) Mean absolute bias/mean bias and (top right) max/min/RMSE. Stippling indicates 5% level of significance.

c. *South Asian monsoon*

Winds within the South Asian monsoon (SAM) region (20°S–30°N, 40°–140°E) are influenced by the migrating ITCZ and land–sea thermal contrasts. In addition to drastic seasonal changes in wind direction, this region is characterized by large seasonal wind speed PDF oscillations. The range in monthly climatological wind speed and shape within the Somali jet region is the largest of all other oceanic locations (Fig. 8, left). During NH summer, the southerly winds of the Somali jet prevail off the coast of Somalia and the Arabian Peninsula (Chang et al. 2004). These winds are strong (mean speed ~11 m s^{-1}) and persistent (standard deviation ~2 m s^{-1}), resulting in high shape values ~7 (Fig. 8, right). In contrast, weaker (mean ~4 m s^{-1}) and slightly more variable northerly winds occur throughout the rest of the year, resulting in lower shape values.

SAM region mean wind speed, standard deviation, and shape biases are strongly seasonal (Fig. 9). Winds in the South China Sea and Bay of Bengal are approximately 3 m s^{-1} too fast (slow) in winter (summer). Meehl et al. (2006) note this same bias. Similarly, winds are too gusty (too persistent) (about 2 m s^{-1}) in winter (summer). NH summer negative shape biases exist within the Bay of Bengal (shape biases $\lesssim -3$) and the eastern Arabian Sea. In contrast, NH summer positive shape biases exist within the Somali jet ($\gtrsim 3.5$) where mean winds are also too fast (up to 1 m s^{-1}) and variability is underestimated. Positive wind speed and

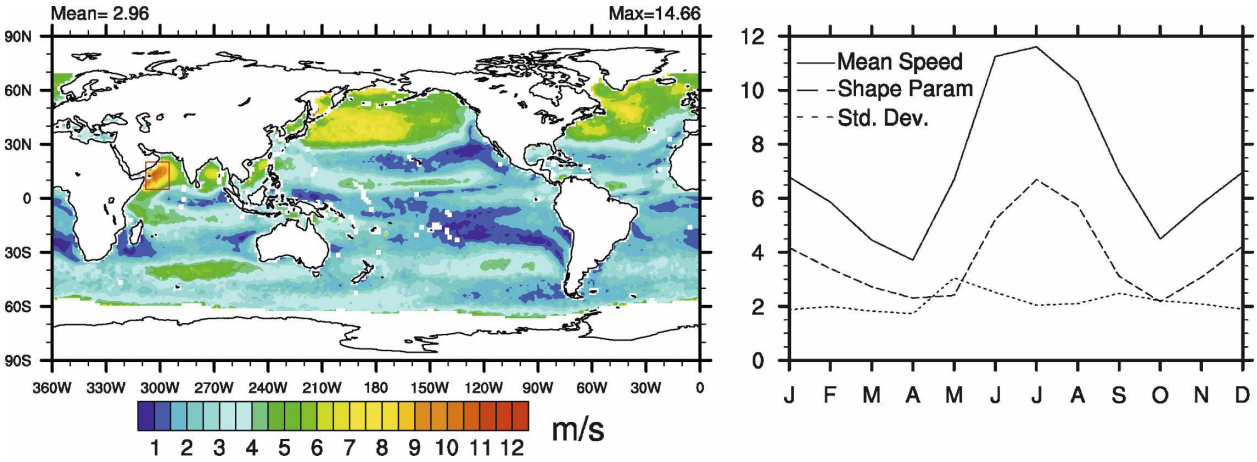

FIG. 8. (left) QuikSCAT 2000–05 seasonal cycle wind speed range (max − min). (right) Somali jet region (5°–20°N, 295°–308°W) area-averaged monthly climatological wind speed mean, shape, and standard deviation.

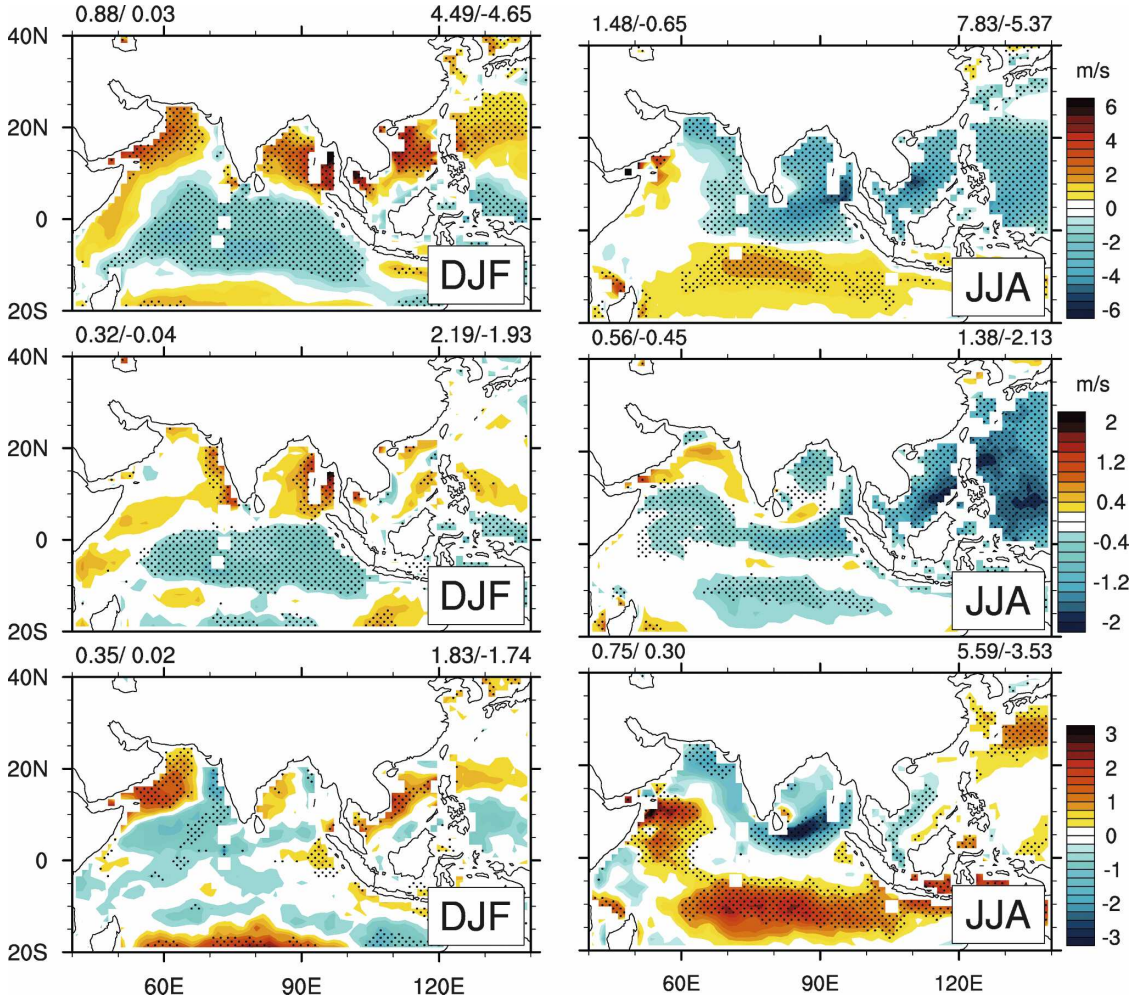

FIG. 9. Northern Hemisphere (left) winter and (right) summer (top) climatological mean, (middle) standard deviation, and (bottom) shape biases (CAM − QuikSCAT): 5% level of significance stippled.

shape biases of about 2 m s^{-1} and 2 occur near 10°S, just south of the southern ITCZ. The simulated cross-equatorial mean wind speeds near the Somalian coast agree well with QuikSCAT. However, this region has moderate positive shape biases (~1).

In NH winter the largest mean wind speed biases are in the South China Sea and Bay of Bengal. Too fast winds (~2.0 m s^{-1}) in the western Arabian Sea coupled with near-zero standard deviation biases result in collocated positive shape biases of ~1.25. Winds are ~2 m s^{-1} too fast in eastern Indonesia in both seasons. QuikSCAT measurements in this region may experience island and reef effects on ocean surface roughness. The central and western Indian Ocean suffer from extensive though moderate wind speed and shape biases ($\lesssim$2 m s^{-1} and 1, respectively).

d. TAO/TRITON region

The TAO/TRITON region (9°S–9°N, 135°E–90°W) is dominated by the Pacific warm pool, ITCZ, and northern branch of the South Pacific convergence zone (SPCZ). The TAO buoys sense wind speed and shape maxima that are associated with seasonally migrating trade wind incursions near 5°N and 5°S (Fig. 10). Slow, positively skewed winds (shape $\lesssim$ 3.6) migrate meridionally with the ITCZ and, thus, spend more time in the NH. This is in contrast to the wind speed standard deviation whose pattern is relatively stationary. The SPCZ characterized by low wind speed means and higher variability (low shape values) is seen south of 5°S.

Differences between QuikSCAT retrievals and in situ measurements (corrected for ocean currents) help to indicate the measurement uncertainty. Many studies examine QuikSCAT differences between TAO and research vessel data (Chelton and Freilich 2005; Ebuchi et al. 2002; Weissman et al. 2002). Differences <1 m s^{-1} are considered within the measurement uncertainty. The correction for ocean currents applied to the TAO/TRITON buoy measurements reduces these differences (Kelly et al. 2005). Despite the drastic differences in measurement methods, QuikSCAT and TAO observations agree well. Mean wind speed differences (QuikSCAT − TAO) are between 0.58 and −0.51 m s^{-1}, shape differences between 0.67 and −0.56, and standard deviation differences between 0.06 and −0.50 m s^{-1} (Fig. 10, second row). Differences in 90th percentile speed are higher, between 0.58 and −1.04 m s^{-1}. This is consistent with the high frequency of TAO sampling relative to QuikSCAT and the slight decline of QuikSCAT accuracy with high winds. Faster and more persistent QuikSCAT winds near 5°N and 5°S result in collocated positive shape differences. These faster QuikSCAT wind speeds are consistent with the findings of Jiang et al. (2005). In contrast, QuikSCAT winds along the equator are slower with near-zero shape and standard deviation differences.

The GCM underestimates zonal-average wind speeds by up to 2.26 m s^{-1} during the NH winter and spring months (Fig. 10). This exceeds the 0.5 m s^{-1} QuikSCAT versus TAO differences reported by Kelly et al. (2001) and thus cannot be attributed to measurement uncertainties. The SPCZ, eastern Pacific cold tongue, and northern ITCZ (8°N) have slower simulated NH winter mean and 90th percentile winds. Simulated 90th percentile wind speeds are too slow by up to 3.50 m s^{-1} throughout the ITCZ seasonal cycle.

Negative shape biases in excess of 1.0 occur during NH winter while positive biases larger than 1.0 occur the rest of the year (Fig. 10). Too high shape value biases along the northern and southern ITCZ bounds are connected to the GCM overestimate of subtropical subsidence (Hurrell et al. 2006). Excessive subsidence can exaggerate trade wind strength and persistence, resulting in a more negatively skewed wind speed PDF. Shape biases throughout the summer and fall also appear to be related to the GCM's unrealistically strong convection within the southern ITCZ. The positive shape bias of 2.6 in May is due to a lag between the simulated and observed NH trade wind northward migration (Fig. 10).

4. Representing subgrid-scale wind speeds

The momentum flux is greater when computed from the full wind speed distribution than from the mean wind speed alone (section 3a). Additionally, smaller sensible and latent heat flux responses (not shown) of varying sign are realized over the oceans with significant responses within the western boundary current regions. When integrated over a multiyear time period these surface flux responses alter climate features, such as atmospheric stability and tropospheric circulation. We now allow these instantaneous responses to feed back throughout the climate and examine the impact on wind speed statistic biases found above. CAM3 is integrated over 2000–05 using a four-bin wind speed PDF (as in section 3a). However, four-bin weighted average fluxes are now exchanged between the land, lake, atmosphere, ocean, and ice components.

The largest CAM3 bias improvements (summarized in Table 1) are realized with wind speed PDFs predicted using a C_k of 1.05. Surface flux improvements are expected to be gained from subgrid-scale wind speed

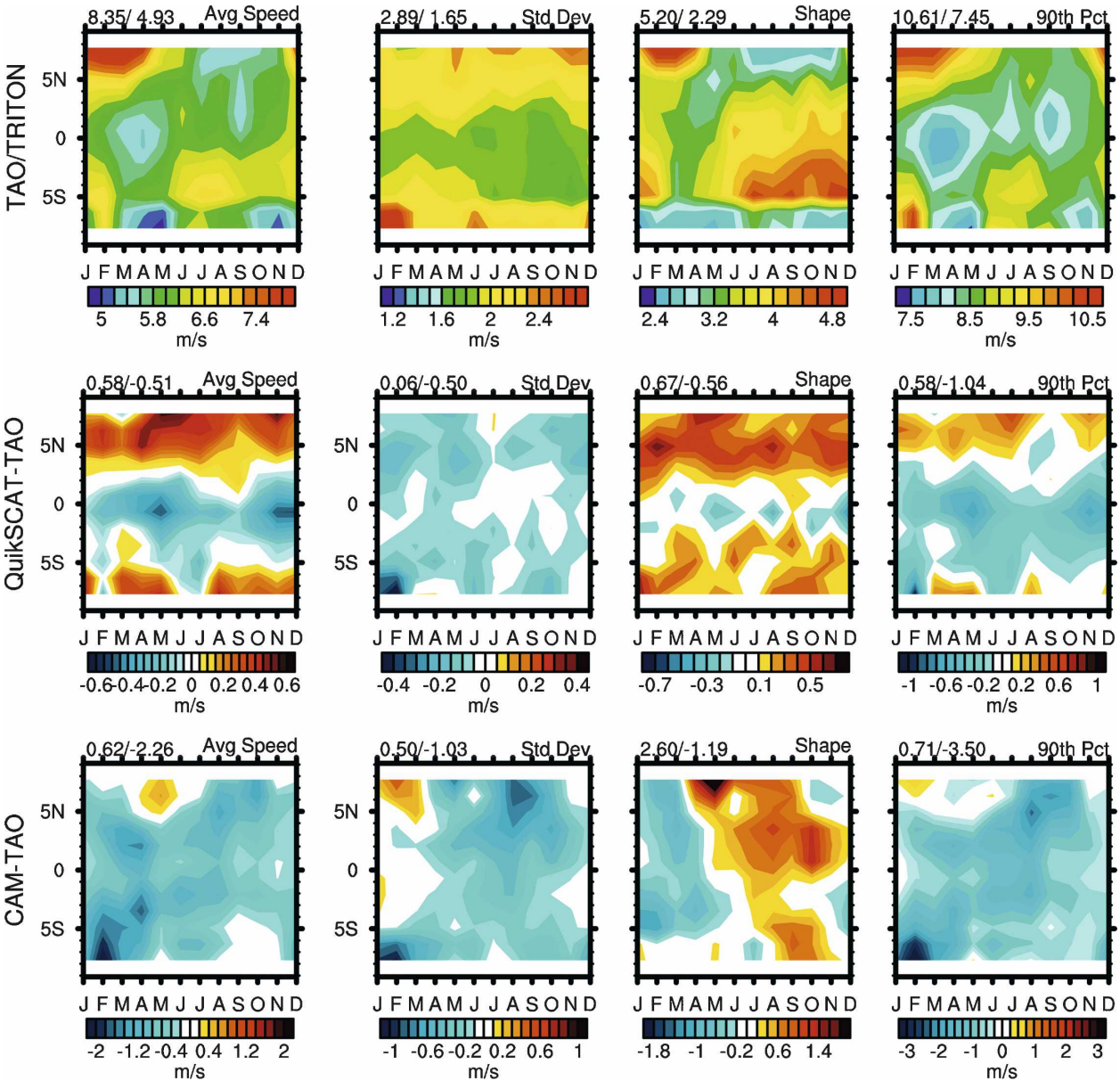

FIG. 10. (top) 2000–05 monthly zonal mean TAO array 10-m wind speed mean, shape, standard deviation, and 90th percentile; differences (middle) QuikSCAT − TAO and (bottom) CAM − TAO. Note difference in scales.

variability representation. Moreover, it is not surprising to find resulting tropospheric circulation improvements. CAM3 NH winter SLP biases (CAM3 − NCEP-2) are similar to those reported by Hurrell et al. (2006) (Fig. 11, left). With the inclusion of a four-bin wind speed PDF, the December–February (DJF) global mean absolute bias is reduced from 2.57 to 1.83 hPa. Positive CAM3 SLP biases within the subtropics are reduced across all seasons (not shown). Especially noteworthy are the SLP improvements in the region occupied by the Aleutian low. Further, negative SLP biases poleward of 50°S improve in most regions, with drastic improvements in the Arctic regions. Significant collocated 500-hPa geopotential height bias reductions are also found (Fig. 11, right). The DJF 500-hPa height global mean absolute bias is reduced from 33.01 to 25.86 gpm.

With significant SLP improvements, we expect to see improvements in surface wind speed statistics (summarized in Table 1). Global mean absolute wind speed, standard deviation, shape, and 90th percentile speed biases are reduced from 0.67 to 0.58 m s^{-1}, from 0.24 to

TABLE 1. 2000–05 global mean absolute biases and percent changes.

	CAM3	CAM3 four-bin PDF	Change (%)
Wind speed mean (m s^{-1})	0.67	0.58	−13.43
Wind speed std dev (m s^{-1})	0.24	0.20	−16.67
Wind speed shape parameter	0.36	0.34	−5.56
Wind speed 90th percentile (m s^{-1})	0.80	0.62	−22.50
Sea level pressure (hPa)	2.52	2.13	−15.48
DJF sea level pressure (hPa)	2.57	1.83	−28.79
500-hPa geopotential height (gpm)	31.67	27.66	−12.66
DJF 500-hPa geopotential height (gpm)	33.01	25.86	−21.66

0.20 m s^{-1}, from 0.36 to 0.34 m s^{-1}, and from 0.80 to 0.62 m s^{-1}, respectively (Fig. 12). Root-mean-square errors and maximum biases are reduced for all statistics. Positive biases, regardless of their location, are reduced for all statistics. In contrast, negative biases within the tropics and western boundary currents worsened slightly both in spatial extent and magnitude for all statistics.

5. Discussion

The majority of GCM wind speed biases are identified with known climate features such as the subtropical anticyclones, storm tracks, and ITCZ. Thus, it is not surprising that we have found evidence linking these biases to tropospheric circulation and thermodynamic GCM biases reported by previous studies. Large NH summer positive mean wind speed and shape biases are found within the NH trade wind regions, consistent with subtropical anticyclone location and strength biases. Winter storm tracks are dominated by large positive wind speed mean, 90th percentile speed, and standard deviation biases consistent with negative storm track SLP biases reported in other studies (Hurrell et al. 2006). Representing subgrid-scale surface wind speed variability reduces SLP and 500-hPa height biases considerably. However, a portion of these dynamics-related GCM wind biases are likely to persist until the GCM large-scale circulation improves. Additionally, year-round negative wind speed mean, 90th percentile speed, and shape biases within the ITCZ are consistent with overactive GCM convection (Dai and Trenberth 2004; Rasch et al. 2006). Unlike the SLP and 500-hPa height biases, these are exacerbated when subgrid-scale wind speed variability is included.

The primary climatological wind bias is in the storm tracks of both hemispheres where the westerlies are >1 m s^{-1} too fast. These biases, also noted in earlier studies (Hurrell et al. 2006; Collins et al. 2006b; Hack et al. 2006), are symptomatic of underestimated surface drag by fast, subgrid-scale winds. Surface momentum flux has a nonlinear, convex relationship with wind speed (Wright and Thompson 1983). Thus, the momentum flux predicted by the mean wind speed of a wind PDF

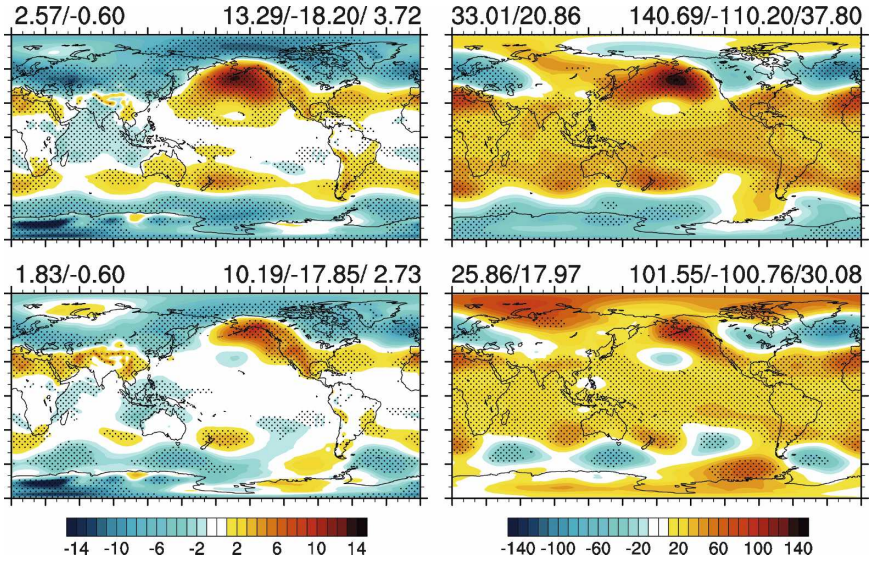

FIG. 11. 2000–05 mean DJF (left) sea level pressure (hPa) and (right) 500-hPa geopotential height differences (gpm). (top) CAM3 − NCEP-2 and (bottom) CAM3 four-bin wind speed PDF − NCEP-2. (top left) Mean absolute bias/mean bias and (top right) max/min/RMSE. Stippling indicates 5% level of significance.

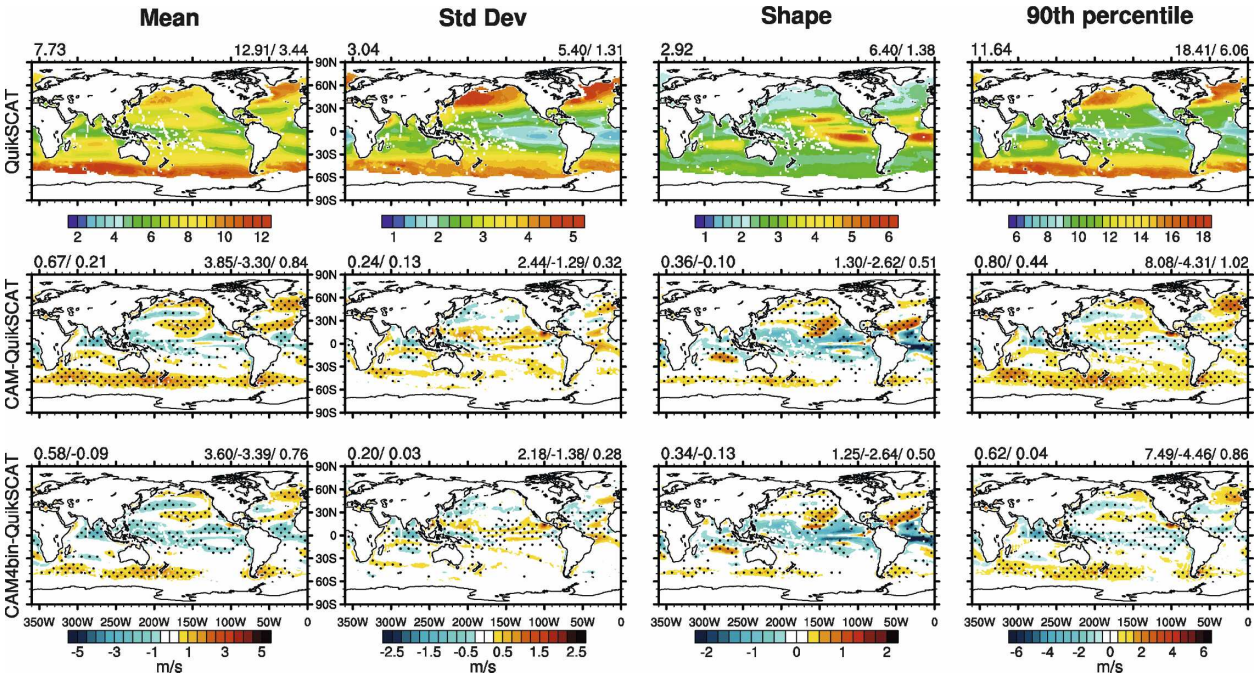

FIG. 12. As in Fig. 2 but for (middle) CAM3 − QuikSCAT and (bottom) CAM3 four-bin wind speed PDF − QuikSCAT.

is less than the mean momentum flux of the fully resolved wind PDF. We have confirmed this with offline, single-column sensitivity studies of the air–sea fluxes in equilibrium with single-bin and multibin wind PDFs. By representing wind speed variability within a GCM and allowing for feedbacks, we have reduced SLP and 500-hPa geopotential height biases in many regions throughout the globe. Most notable are the dramatic improvements associated with the Aleutian low during NH winter. A significant reduction in surface wind speed biases resulted from both increased drag and improved tropospheric circulation.

The ITCZ is dominated by year-round negative GCM shape and mean wind speed biases. Further, with the exception of the positive trade biases, mean and 90th percentile wind speeds are slower year-round within the TAO region. The too-slow winds along the ITCZ may be a generic bias in tropical convection simulations. This study shows that the bias appears in the CAM3 GCM (see also Hack et al. 2006) as well as NCEP-2. Chelton and Freilich (2005) describe this bias in the ECMWF operational numerical weather prediction model. The CAM3-simulated convection in this region is overactive (Dai and Trenberth 2004; Rasch et al. 2006) and moves surface vapor aloft too efficiently. This enhanced convection increases surface wind variability and precipitation. As a result, the GCM overestimates convective rainfall and underestimates stratiform rain in the tropics (Rasch et al. 2006), although the total tropical precipitation agrees reasonably well with observations.

This assessment of observed and predicted wind speed PDFs suggests future avenues of research to reduce model biases. Predicting physically based wind speed PDFs is one avenue. This improves surface fluxes of mineral dust over land (e.g., Cakmur et al. 2004), which, like momentum fluxes, increase nonlinearly with wind speed. Such methods may well improve air–sea exchange too. Boundary layer conditions, which could be used to diagnose subgrid-scale wind speed variability, include mechanical (wind shear) and thermodynamic (buoyancy driven) turbulence, Richardson number, Deardorff velocity, and moist convection. Most GCMs provide these diagnostics, although more research is necessary to understand their connection to surface wind PDFs (Panofsky et al. 1977; Cakmur et al. 2004). Assessing climate sensitivity to wind speed component (zonal and meridional) variability is another avenue.

6. Conclusions

We characterized and intercompared 2000–05 surface wind speed probability density functions (PDFs) from QuikSCAT measurements, NCEP-2 reanalysis, TAO/TRITON buoys (TAO), and CAM3 GCM predictions. The datasets were spatially and temporally regridded and filtered to make the comparisons equi-

table. Some intrinsic differences remained, however, such as the distinction between QuikSCAT instantaneous measurements and the GCM and reanalysis time steps (10 min and 6 h, respectively). Global and regional 6-yr wind speed mean, 90th percentile wind speed, standard deviation, and Weibull shape parameter climatologies were examined. Overall, the PDFs from measurements, despite their methodological, spatial, and temporal sampling differences, are in much closer agreement with one another than with the GCM predictions.

Swaths of homogeneous wind speed statistics accompany large-scale climate features such as the subtropical anticyclones, ITCZ, and storm tracks. As expected, wind speed mean, 90th percentile winds and variance peak within the wintertime storm tracks. Further, Southern Hemisphere (SH) storm track wind speed statistics vary less intraannually compared to the Northern Hemisphere (NH). The trade wind regions that bound the northern and southern extent of the ITCZ are characterized by moderate wind speeds, low variability, and high shape values. We identify an approximately stationary pattern to the wind speed variance in the equatorial Pacific. Interestingly, a distinct wind speed mean and shape anomaly migrates with the ITCZ across this stationary background. The region with the largest seasonal-mean wind speed and shape variability is the Somali jet.

NCEP-2 overestimates QuikSCAT measurements within the extratropics over most statistics examined, with peak differences found in the storm tracks. The tropics were characterized by negative or near-zero differences for both NCEP-2 and the GCM. Negative shape parameter differences were found throughout most of the globe with the largest differences in the tropics. Negative (NCEP-2 minus QuikSCAT) shape parameter differences were found throughout the global ocean regions and were nearly zero within the storm tracks.

The GCM-predicted wind speed PDFs agree well with QuikSCAT and the other observations in most seasons and regions. Surface wind speed PDFs are dependent upon atmospheric boundary layer (ABL) stability and large-scale circulations. Thus, our intercomparison between observed and predicted global winds suffers most from dataset and model limitations near fast ocean currents, sea surface temperature fronts, and regions where ABL stability deviates from neutral. However, most GCM biases that we identify cannot be attributed entirely to such methodological limitations. The primary climatological wind bias in the GCM occurs in the storm tracks of both hemispheres where the westerlies are >1 m s^{-1} too fast.

Owing to the nonlinear response of surface fluxes to wind speed, it is important to understand subgrid-scale wind speed variability and to represent it accurately in GCMs. A first step for models is to quantify their wind variability performance against high-resolution observations such as QuikSCAT and TAO/TRITON. Tropospheric circulation and wind speed statistics were improved in many regions with the representation of subgrid-scale wind speed variability. At the same time, initiatives such as the Coupled Boundary Layers Air–Sea Transfer (CBLAST) Defense Research Initiative (Edson et al. 2007) are investigating the importance of surface features such as wave breaking on the air–sea transfer of surface fluxes. Improved surface transfer parameterizations derived from such studies will help highlight biases and further improve models.

Acknowledgments. Level 3 QuikSCAT data were obtained from NASA's Jet Propulsion Laboratory (online at http:// podaac.jpl.nasa.gov). TAO project office director M. J. McPhaden provided TAO buoy data. NCEP-2 data are provided by the NOAA/OAR/ESRL PSD, Boulder, Colorado (online at http://www.cdc.noaa.gov). Daniel Wang (UCI) helped with temporal filtering and Dennis Shea (NCAR) graciously supplied SST data. Three anonymous reviewers and the associate editor provided very constructive criticisms and suggestions. This research is supported by NSF ATM-0321380 and IIS-0431203.

APPENDIX

Equal-Probability Wind Speed Bin Methodology

The Weibull PDF is analytically integrable, resulting in a cumulative distribution function (CDF)

$$W(U_{\rm t}, n) = \int_{U_{\rm t}}^{\infty} U^n \left(\frac{k}{c}\right)\left(\frac{U}{c}\right)^{k-1} \exp\left[-\left(\frac{U}{c}\right)^k\right] dU, \tag{A1}$$

where k and c are the shape and scale, and U, $U_{\rm t}$, and n are wind speed, wind speed threshold, and moment number. With a change of variables a condensed version of the CDF above is formulated using the gamma ($U_t = 0$ m s^{-1}) and upper incomplete gamma function ($U_t > 0$ m s^{-1})

$$W(U_t, n) = c^n \Gamma\left[\frac{k+n}{k}, \left(\frac{U_t}{c}\right)^k\right]. \tag{A2}$$

The probability of a wind speed exceeding a threshold U_t is given by

$$p(U > U_t) = \exp\left[-\left(\frac{U_t}{c}\right)^k\right], \tag{A3}$$

and $p(U < U_t) = 1 - p(U > U_t)$. Inverting and solving Eq. (A3) for U_t we can calculate the wind speed U_i at which a fraction p_i of the PDF exceeds U_i

$$U_i = c(-\ln p_i)^{1/k}. \quad \text{(A4)}$$

Thus, upper $U_{i,\max}$ and lower $U_{i,\min}$ bin limits for each bin are calculated using

$$U_{i,\min} = c[-\ln(1 - p_{i,\min})]^{1/k}, \quad \text{(A5)}$$

$$U_{i,\max} = c[-\ln(1 - (p_{i,\min} + 1/4))]^{1/k}. \quad \text{(A6)}$$

Four mean wind speeds corresponding to the four bins (truncated PDFs) are calculated. The mean wind speed for each truncated PDF is equal to the first moment of the truncated PDF normalized by the wind speed interval probability

$$\overline{U}_i = \frac{W(U_{i,\min}, 1) - W(U_{i,\max}, 1)}{W(U_{i,\min}, 0) - W(U_{i,\max}, 0)}. \quad \text{(A7)}$$

REFERENCES

Bentamy, A., E. Autret, P. Queffeulou, and Y. Quilfen, 2000: Intercomparison of ERS-2 and QuickSCAT winds. *Proc. IGARSS,* **1,** 234–236.

Bourassa, M. A., D. M. Legler, J. J. O'Brien, and S. R. Smith, 2003: SeaWinds validation with research vessels. *J. Geophys. Res.,* **108,** 3019, doi:10.1029/2001JC001028.

Cakmur, R. V., R. L. Miller, and O. Torres, 2004: Incorporating the effect of small-scale circulations upon dust emission in an atmospheric general circulation model. *J. Geophys. Res.,* **109,** D07201, doi:10.1029/2003JD004067.

Chang, C.-P., and Coauthors, 2004: *East Asian Monsoon.* Vol. 2. World Scientific, 564 pp.

Chelton, D. B., and M. H. Freilich, 2005: Scatterometer-based assessment of 10-m wind analyses from the operational ECMWF and NCEP numerical weather prediction models. *Mon. Wea. Rev.,* **133,** 409–429.

——, M. G. Schlax, M. H. Freilich, and R. F. Milliff, 2004: Satellite radar measurements reveal short-scale features in the wind stress field over the world ocean. *Science,* **303,** 978–983.

Collins, W. D., and Coauthors, 2004: Description of the NCAR community atmosphere model (CAM 3.0). NCAR Tech. Note NCAR/TN-464+STR, 226 pp.

——, and Coauthors, 2006a: The Community Climate System Model: CCSM3. *J. Climate,* **19,** 2122–2143.

——, and Coauthors, 2006b: The formulation and atmospheric simulation of the Community Atmosphere Model version 3 (CAM3). *J. Climate,* **19,** 2144–2161.

Dai, A., and K. E. Trenberth, 2004: The diurnal cycle and its depiction in the Community Climate System Model. *J. Climate,* **17,** 930–951.

Donelan, M., W. Drennan, E. Saltzman, and R. Wanninkhof, 2002: *Gas Transfer at Water Surfaces.* Amer. Geophys. Union, 383 pp.

Ebuchi, N., H. C. Graber, and M. J. Caruso, 2002: Evaluation of wind vectors observed by QuikSCAT/SeaWinds using ocean buoy data. *J. Atmos. Oceanic Technol.,* **19,** 2049–2062.

Edson, J., and Coauthors, 2007: The Coupled Boundary Layers and Air–Sea Transfer Experiment in low winds. *Bull. Amer. Meteor. Soc.,* **88,** 341–356.

Feely, R. A., R. Wanninkhof, W. McGillis, M.-E. Carr, and C. E. Cosca, 2004: Effects of wind speed and gas exchange parameterizations on air-sea CO_2 fluxes in the equatorial Pacific Ocean. *J. Geophys. Res.,* **109,** C08S03, doi:10.1029/2003JC001896.

Gillette, D. A., and R. Passi, 1988: Modeling dust emission caused by wind erosion. *J. Geophys. Res.,* **93** (D11), 14 233–14 242.

Hack, J. J., J. M. Caron, G. Danabasoglu, K. W. Oleson, C. Bitz, and J. E. Truesdale, 2006: CCSM–CAM3 climate simulation sensitivity to changes in horizontal resolution. *J. Climate,* **19,** 2267–2289.

Hoffman, R. N., and S. M. Leidner, 2005: An introduction to the near-real-time QuikSCAT data. *Wea. Forecasting,* **20,** 476–493.

Hurrell, J. W., J. J. Hack, A. S. Phillips, J. Caron, and J. Yin, 2006: The dynamical simulation of the Community Atmosphere Model version 3 (CAM3). *J. Climate,* **19,** 2162–2183.

Jiang, C., M. F. Cronin, K. A. Kelly, and L. Thompson, 2005: Evaluation of a hybrid satellite- and NWP-based turbulent heat flux product using Tropical Atmosphere–Ocean (TAO) buoys. *J. Geophys. Res.,* **110,** C09007, doi:10.1029/2004JC002824.

Justus, C. G., W. R. Hargraves, A. Mikhail, and D. Graber, 1978: Methods for estimating wind speed frequency distributions. *J. Appl. Meteor.,* **17,** 350–353.

——, K. Mani, and A. S. Mikhail, 1979: Interannual and month-to-month variations of wind speed. *J. Appl. Meteor.,* **18,** 913–920.

Kanamitsu, M., W. Ebisuzaki, J. Woollen, S.-K. Yang, J. J. Hnilo, M. Fiorino, and G. L. Potter, 2002: NCEP–DOE AMIP-II Reanalysis (R-2). *Bull. Amer. Meteor. Soc.,* **83,** 1631–1643.

Kelly, K. A., S. Dickinson, M. J. McPhaden, and G. C. Johnson, 2001: Ocean currents evident in satellite wind data. *Geophys. Res. Lett.,* **28,** 2469–2472.

——, ——, and G. C. Johnson, 2005: Comparisons of scatterometer and TAO winds reveal time-varying surface currents for the tropical Pacific Ocean. *J. Atmos. Oceanic Technol.,* **22,** 735–745.

Liu, W. T., and W. Tang, 1996: Equivalent neutral wind. NASA Jet Propulsion Laboratory Publication 96-17, 20 pp.

——, and X. Xie, 2002: Double intertropical convergence zones—A new look using scatterometer. *Geophys. Res. Lett.,* **29,** 2072, doi:10.1029/2002GL015431.

Mears, C. A., D. K. Smith, and F. J. Wentz, 2001: Comparison of special sensor microwave imager and buoy-measured wind speeds from 1987 to 1997. *J. Geophys. Res.,* **106** (11), 719–729.

Meehl, G. A., J. M. Arblaster, D. M. Lawrence, A. Seth, E. K. Schneider, B. P. Kirtman, and D. Min, 2006: Monsoon regimes in the CCSM3. *J. Climate,* **19,** 2482–2495.

Monahan, A. H., 2006a: The probability distribution of sea surface wind speeds. Part I: Theory and SeaWinds observations. *J. Climate,* **19,** 497–520.

——, 2006b: The probability distribution of sea surface wind speeds. Part II: Dataset intercomparison and seasonal variability. *J. Climate,* **19,** 521–534.

O'Neill, L. W., D. B. Chelton, and S. K. Esbensen, 2005: High-resolution satellite measurements of the atmospheric boundary layer response to SST variations along the Agulhas return current. *J. Climate,* **18,** 2706–2723.

Panofsky, H. A., H. Tennekes, D. H. Lenschow, and J. C. Wyngaard, 1977: The characteristics of turbulent velocity components in the surface layer under convective conditions. *Bound.-Layer Meteor.,* **11,** 355–361.

Pavia, E. G., and J. J. O'Brien, 1986: Weibull statistics of wind speed over the ocean. *J. Climate Appl. Meteor.,* **25,** 1324–1332.

Rasch, P. J., and Coauthors, 2006: A characterization of tropical transient activity in the CAM3 atmospheric hydrologic cycle. *J. Climate,* **19,** 2222–2242.

Reynolds, R. N., T. Smith, D. Stokes, and W. Wang, 2002: An improved in situ and satellite SST analysis for climate. *J. Climate,* **15,** 1609–1625.

Wang, C., R. H. Weisberg, and H. Yang, 1998: Effects of the wind speed–evaporation–SST feedback on the El Niño–Southern Oscillation. *J. Atmos. Sci.,* **56,** 1391–1403.

Wanninkhof, R., S. C. Doney, T. Takahashi, and W. R. McGillis, 2002: The effect of using time-averaged winds on regional air-sea CO_2 fluxes. *Gas Transfer at Water Surfaces, Geophys. Monogr.,* Vol. 127, Amer. Geophys. Union, 351–356.

Weissman, D. E., M. A. Bourassa, and J. Tongue, 2002: Effects of rain rate and wind magnitude on SeaWinds scatterometer wind speed errors. *J. Atmos. Oceanic Technol.,* **19,** 738–746.

Wright, D. G., and K. R. Thompson, 1983: Time-averaged forms of the nonlinear stress law. *J. Phys. Oceanogr.,* **13,** 341–345.

Yuan, X., 2004: High-wind-speed evaluation in the southern ocean. *J. Geophys. Res.,* **109,** D13101, doi:10.1029/2003JD004179.